Wang *et al. Microstructures* **2025**, *5*, 2025088
DOI: 10.20517/microstructures.2025.33

Microstructures

Research Article

Open Access

Enhanced strength and ductility of high-entropy alloy via dislocation-mediated heterogeneous martensitic transformation

Feng Wang[1,#], Xinglong An[1,#], Zhangwei Wang[1], Wenqian Wu[2], Wenzhen Xia[3], Song Ni[1], Ji Gu[1], Jianhong Yi[4], Yong Yang[5,6], Min Song[1], Yuntian Zhu[6]

[1]State Key Laboratory of Powder Metallurgy, Central South University, Changsha 410083, Hunan, China.
[2]Department of Mechanical and Materials Engineering, University of Nebraska-Lincoln, Lincoln, NE 68588, USA.
[3]School of Metallurgical Engineering, Anhui University of Technology, Ma'anshan 243002, Anhui, China.
[4]School of Materials Science and Engineering, Kunming University of Science and Technology, Kunming 650093, Yunnan, China.
[5]Department of Mechanical Engineering, College of Engineering, City University of Hong Kong, Kowloon Tong 999077, Hong Kong, China.
[6]Department of Materials Science and Engineering, College of Engineering, City University of Hong Kong, Kowloon Tong 999077, Hong Kong, China.
[#]Authors contributed equally.

Correspondence to: Prof. Zhangwei Wang and Prof. Min Song, State Key Laboratory of Powder Metallurgy, Central South University, No. 932 Lushan South Road, Changsha 410083, Hunan, China. E-mail: z.wang@csu.edu.cn, msong@csu.edu.cn; Prof. Yuntian Zhu, Department of Materials Science and Engineering, College of Engineering, City University of Hong Kong, No. 83 Tat Chee Avenue, Kowloon Tong 999077, Hong Kong, China. E-mail: y.zhu@cityu.edu.hk

How to cite this article: Wang, F.; An, X.; Wang, Z.; Wu, W.; Xia, W.; Ni, S.; Gu, J.; Yi, J.; Yang, Y.; Song, M.; Zhu, Y. Enhanced strength and ductility of high-entropy alloy via dislocation-mediated heterogeneous martensitic transformation. *Microstructures* **2025**, *5*, 2025088. https://dx.doi.org/10.20517/microstructures.2025.33

Received: 14 Mar 2025 **First Decision:** 12 May 2025 **Revised:** 16 May 2025 **Accepted:** 21 May 2025 **Published:** 7 Aug 2025

Academic Editor: Nima Haghdadi **Copy Editor:** Xing-Yue Zhang **Production Editor:** Xing-Yue Zhang

Abstract

The pursuit of unparalleled mechanical properties has driven the exploration of heterostructured materials in recent years. Traditional strategies that rely on tuning internal plastic strain to create heterogeneous distributions of martensite have failed to overcome the strength-ductility trade-off in materials, despite the desirable extensive hardening effect of martensitic transformation. Here, we report a paradigm-shifting approach utilizing dislocation-mediated heterogeneous martensitic transformation to resolve this dilemma. Realized in a partially recrystallized metastable face-centered cubic (FCC) high-entropy alloy (HEA), the phase transformation from FCC to a hexagonal close-packed (HCP) structure occurs exclusively in the non-recrystallized zones during initial tensile loading, facilitated by abundant pre-existing dislocations serving as sources for partial dislocations. In contrast, deformation in the adjacent recrystallized zones, which are devoid of dislocations, proceeds through dislocation

slip. The resulting heterogeneous deformation persists with increasing strain, underpinned by the emergence of unique dual FCC-HCP nanograins at localized HCP lamellar intersections in the non-recrystallized zones. Such sustained heterogeneous deformation enables the full exploitation of remarkable hetero-deformation-induced strengthening and strain hardening, leading to a superior strength-ductility combination in the current HEA. Our findings establish a new pathway for engineering high-performance heterostructured materials.

Keywords: Heterogeneous martensitic transformation, high-entropy alloy, strength, ductility, hetero-deformation induced hardening

INTRODUCTION

Heterostructured materials, defined by a disparity in microstructural features that lead to strength heterogeneity across their various zones, have garnered widespread attention due to their promising mechanical properties[1,2]. The foundation of this enhanced mechanical performance lies in hetero-deformation induced (HDI) strengthening and strain hardening, phenomena that emerge from the dynamic interplay between the back stress in softer zones and forward stress in harder ones[3,4]. Exploiting this advantageous HDI hardening effect, a plethora of strategies have been implemented in the engineering of heterostructured materials[5]. Notable among these are the creation of heterogeneous lamellar structures comprising ultrafine and coarse grains[6], the establishment of a gradient in grain size[7-9], twin density[10,11], or dislocation density structure[12], and the development of multi-modal configurations that integrate bimodal grain distributions with nanoprecipitates[13-15]. Each of these strategies plays a crucial role in attaining a desirable combination of strength and ductility, pushing the boundaries of material performance.

Deformation-induced martensitic phase transformation stands out as a highly sought-after attribute, primarily due to its role in facilitating progressively intense strain hardening, a cornerstone of the well-known transformation-induced plasticity (TRIP) effect[16,17]. In the realm of heterogeneous material design, the twinning-induced plasticity (TWIP) effect has been widely implemented[10,11], whereas the TRIP effect remains a potential strategy with untapped potential for development. The propensity for martensite phase transformation is largely governed by stacking fault energy (SFE), a parameter intricately linked to alloy composition[18-20]. In this regard, for given metastable alloys, achieving heterogeneous distributions of martensite typically involves tailoring internal plastic strain, as demonstrated through methods like torsion-based treatments[21] or surface nano-crystallization techniques[22]. However, these gradient distributions of martensite, while they significantly enhance strength, often result in a marked reduction in ductility, thereby failing to surmount the compromise between strength and ductility.

Here, we report a pioneering approach utilizing dislocation-mediated martensite phase transformation for the creation of heterostructured materials. We showcase this breakthrough in a heterostructured face-centered cubic (FCC) $Fe_{40}Co_{20}Cr_{20}Mn_{10}Ni_{10}$ high-entropy alloy (HEA), which consists of recrystallized zones with a fine grain size of ~2 μm and non-recrystallized zones with a high density of dislocations. Upon loading, the presence of dislocations and the associated low-angle grain boundaries (LAGBs) within the non-recrystallized zones serves as sources of partial dislocations, initiating martensitic phase transformation. Notably, this hexagonal close-packed (HCP) martensite formation is conspicuously absent in the neighboring recrystallized zones. Such localized transformation underpins the sustained heterogeneous deformation across different zones, effectively leveraging the HDI hardening to achieve superb mechanical properties compared to other FCC HEAs. Our findings thus mark a significant advance toward realizing an enhanced synergy of strength and ductility in structural materials.

MATERIALS AND METHODS

Bulk non-equiatomic $Fe_{40}Co_{20}Cr_{20}Mn_{10}Ni_{10}$ (atomic percent, at.%) high-entropy alloys (HEAs) were synthesized via a vacuum induction melting technique with high-purity raw metals. The as-cast materials were first homogenized at 1,000 °C for 2 h and, subsequently, cold-rolled to a thickness reduction of 85%, followed by annealing at 675 °C for 60 min under an argon atmosphere. All the heat treatment processes were followed by water quenching.

The FEI Helios Nanolab G3 UC, Zeiss sigma 500 and Zeiss Merlin scanning electron microscope (SEM) were employed to perform energy-dispersive X-ray spectroscopy (EDS), electron backscatter diffraction (EBSD), and electron channeling contrast imaging (ECCI) analysis with a 25 kV acceleration voltage, respectively. The deformation substructures were further examined via Titan G2 Cs-corrected transmission electron microscopy (TEM) operated at 300 kV. Specimens for SEM characterization were produced by mechanical grounding, followed by fine polishing using a silica oxide suspension. For TEM observations, thin foil cut from deformed samples was mechanically grounded to 50 μm, and twin-jet electropolished by TenuPol-5 in an electrolyte consisting of 10% perchloric acid and 90% ethanol with a voltage of 35 V at -35 °C. The needle-shape tips at recrystallized and non-recrystallized sites were prepared using an FEI Helios focused ion beam (FIB) with a Xenon plasma ion source. Atom probe tomography (APT) experiments were performed on a LEAP 5000XR with a 52% detection efficiency. The measurements were run in a voltage mode at 70 K, a detection rate of 0.2%, a pulsing rate of 200 kHz, and a pulsing fraction of 20%. AP suite 6.1 was used for data reconstruction and visualization.

Dog-bone-shaped tensile specimens with a gauge length of 8 mm, width of 2 mm, and thickness of 1 mm were fabricated by electrical discharge machining. After the mechanical polishing, three specimens were tensile tested for each condition in a Zwick/Roell Z5.0TN universal testing machine with a strain rate of $10^{-3}\cdot s^{-1}$ at room temperature under extensometer-measured strain control. The loading-unloading-reloading (LUR) tests were carried out on the Instron MTS793. The specimen was first loaded to a design strain (e.g., 2%) with a strain rate of $5 \times 10^{-4}\cdot s^{-1}$, followed by the unloading using a stress control mode to 20 N with a rate of 200 N per min, and further, reloaded to the stress that was the same as previous value before the next unloading. Nanoindentation experiments were performed for various strain samples using the KLA Nano Indenter® G200X, equipped with a diamond Berkovich tip. The nanohardness tests were conducted at a loading rate of 0.05 mN/s and a peak load of 1 mN.

Molecular dynamics (MD) simulations were carried out using LAMMPS code[23] and employing the second nearest-neighbor modified embedded-atom method (2NN MEAM) potential. We constructed a layered model of non-equiatomic $Fe_{40}Co_{20}Cr_{20}Mn_{10}Ni_{10}$ (in at.%) HEAs. The dimension of the middle layer is about $38 \times 50 \times 1$ nm^3 (Lx × Ly × Lz), and the top and bottom layers are $38 \times 25 \times 1$ nm^3 (Lx × Ly × Lz). The x- and y-axes align closely with $[11\bar{2}]$ and [111] directions, respectively, with the z-axis paralleling the $[1\bar{1}0]$ direction. The top and bottom layers, which exhibit a misorientation angle of around 10° relative to the middle layer, maintain identical orientations. Periodic boundary conditions are applied to all three directions. Relaxation of the model is accomplished by using MD simulations for 40 ps at 10 K and energy minimization. The relaxed model is then loaded by uniaxial tension with a constant engineering strain rate of $10^9\cdot s^{-1}$ along the y-axis at 300 K. OVITO software was used to visualize atomic structures.

RESULTS AND DISCUSSION

Initial microstructure

Figure 1 shows the initial microstructures with heterogeneous structure (HS) in the HEA sample after incomplete recrystallization annealing at 675 °C for 60 min (hereafter referred to as HS-HEA). The EBSD

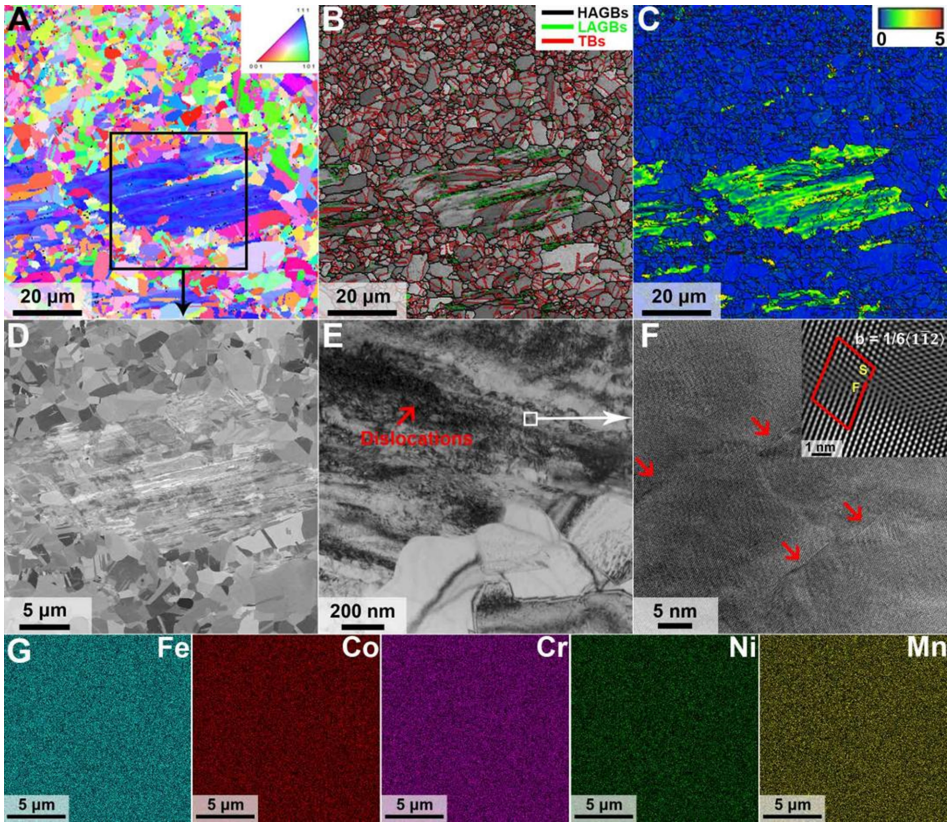

Figure 1. Initial microstructure of the HS-HEA. (A) Inverse pole figure map; (B) Boundary map overlayed with image quality map. High-angle grain boundaries, low-angle grain boundaries, and annealing twin boundaries are highlighted; (C) Kernel average misorientation. These EBSD maps reveal the FCC-structured HS-HEA consisting of both recrystallized and non-recrystallized zones; (D) ECCI image showing the microstructures of the marked zones in (A); (E) Bright-field transmission electron image revealing the non-recrystallized zones with high densities of dislocations; (F) Zoom-in TEM image and the fast Fourier transform filtered high-resolution TEM image of partial dislocation obtained from the areas marked in (E). S and F represent the starting and ending points of Burgers circuit, respectively. b, Burgers vector; (G) SEM-EDS maps of five principal elements, i.e., Fe, Co, Cr, Ni, and Mn, for the zone in (D). All elements are distributed uniformly between recrystallized and non-recrystallized zones. HEA: High-entropy alloy; HS: heterogeneous structure; EBSD: electron backscatter diffraction; FCC: face-centered cubic; ECCI: electron channeling contrast imaging; TEM: transmission electron microscopy; SEM: scanning electron microscope; EDS: energy-dispersive X-ray spectroscopy.

inverse pole figure (IPF) [Figure 1A] and boundary map [Figure 1B] delineate the partially recrystallized HEA containing ~26% area fraction of non-recrystallized zones and ~74% of recrystallized zones, with average grain sizes of ~25 and ~2 μm, respectively. Only high-angle grain boundaries (HAGBs) are detected in the recrystallized zones [Figure 1B], while plenty of LAGBs and dislocations are seen in the non-recrystallized zones, as demonstrated by the EBSD and ECCI [Figure 1C and D]. Cold rolling introduced these dislocations, persisting post-annealing since the temperature was not sufficiently high. Moreover, these dislocations entangle with each other [Figure 1E], which contributes to the formation of LAGBs, leading to pronounced misorientation in non-recrystallized zones [Figure 1C]. The zoom-in high-resolution (HR) TEM image in Figure 1F indicates the existence of numerous Shockley partial dislocations of the $1/6\langle 1\bar{1}2\rangle$ Burgers vector inside the non-recrystallized zones. The SEM-EDS analyses reveal a uniform elemental distribution without any visible component segregation at the microscale [Figure 1G].

In addition, APT measures were further performed to quantify the elemental chemical composition of the recrystallized and non-recrystallized regions at the near-atomic scale. Figure 2 presents the reconstructed 3D atom maps of all elements (Cr, Mn, Fe, Ni and Co), suggesting that the elemental distributions of both

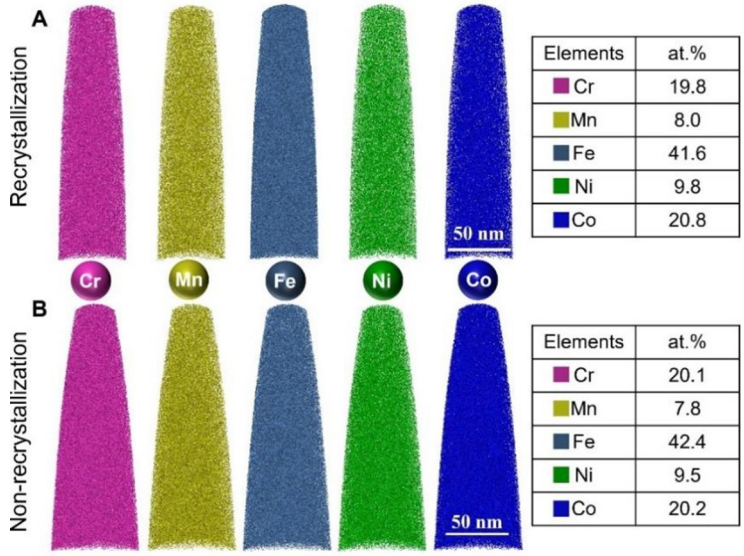

Figure 2. Atom probe tomography images of (A) recrystallized and (B) non-recrystallized zones, showing no obvious chemical composition difference.

regions are completely random without obvious chemical heterogeneity. In order to further identify the potential differences, the actual contents of each element are listed respectively. The experimental data precisely confirms a uniform distribution of all elements, which are close to the nominal compositions, highlighting identical SFE throughout the HEA. Consequently, the subsequent variations of plastic deformation pathways between the recrystallized and non-recrystallized regions are independent of the composition.

Intriguing mechanical performance

Figure 3 presents mechanical testing and analysis of HEAs with different processing conditions. The representative engineering tensile stress-strain curves at room temperature are shown in Figure 3A. Compared to the as-cast HEA in its homogenized state (HM-HEA), the HS-HEA not only demonstrates a substantial increase in yield strength from 165 to 684 MPa, but also produces an impressive rise in tensile elongation from 45% to 49%. This suggests a breakthrough in the notorious strength-ductility trade-off often observed in structural materials[24]. Even when compared with the previously reported exceptional single-phase HEAs, e.g., FeCoCrNiPd HEA[25] and gradient FeCoCrNiMn HEA[26], our HS-HEA showcases better overall mechanical properties. The excellent strength of the HS-HEA stems from the bimodal configuration, which includes both recrystallized zones with fine grains, and non-recrystallized zones filled with high densities of LAGBs and dislocations. The small grain size can enhance the strength due to the Hall-Petch effect[27], while the LAGBs and dislocations provide strong strengthening effects[27], thereby contributing to high yield strength. The quantitative analysis of each strengthening mechanism is provided in the Supplementary Materials.

Notably, in comparison to the HM-HEA, the HS-HEA showcases higher strain hardening rates nearly across the entire deformation regime [Figure 3B]. The high strain hardening further stabilizes the plastic deformation and, thus, dramatically benefits the ductility. The ruptured surface of HS-HEA (inset in Figure 3B) reveals a typical dimpled morphology associated with ductile fracture. Bimodal dimple configuration manifests the heterogeneous stress distribution across different grain sizes during the fracture process. To probe the origin of excellent strain hardening, the LUR tests were conducted [Figure 3C]. As

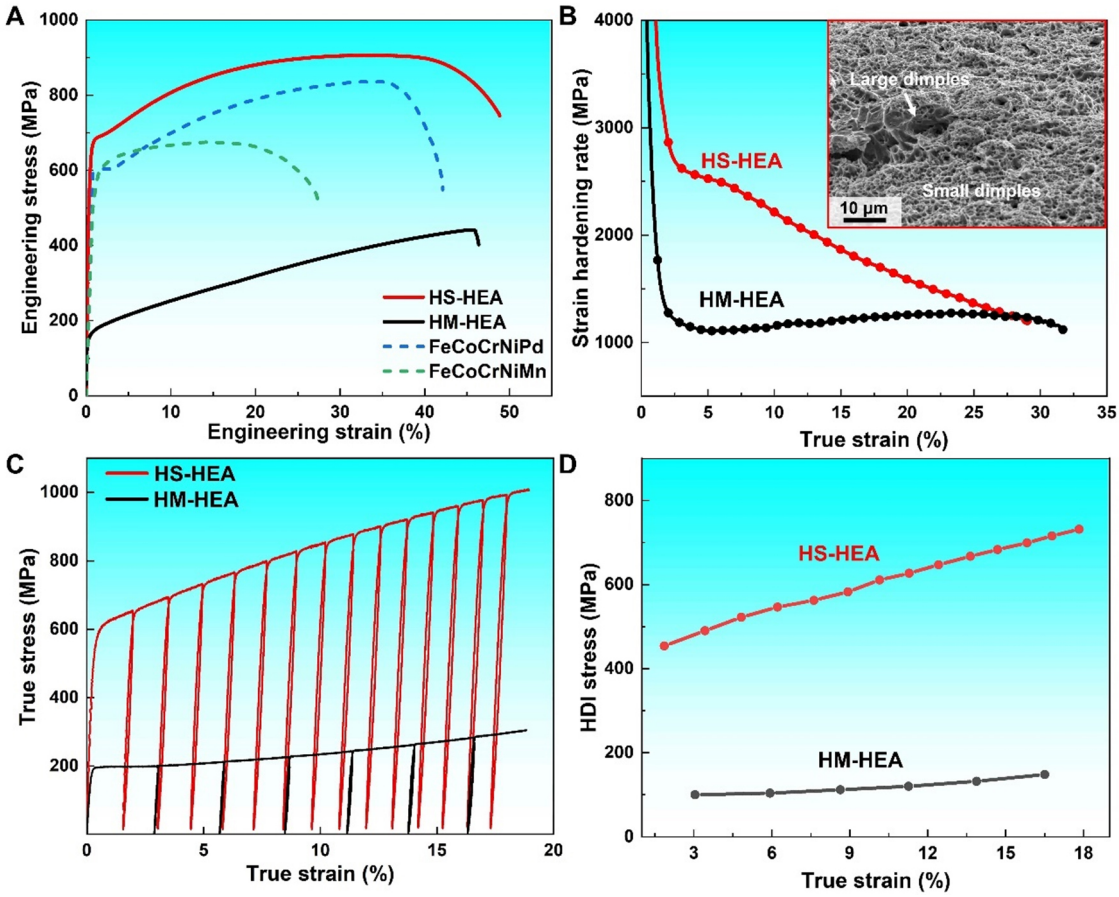

Figure 3. Mechanical performance of HEAs. (A) Engineering stress-strain curves of the HS-HEA and HM-HEA. The mechanical performance of FeCoNiCrPd[25] HEA and gradient FeCoCrNiMn[26] HEA is shown for comparison; (B) Strain hardening rate curves as a function of the true strain for both HS-HEA and HM-HEA. The inserted SEM micrograph shows the ruptured surface of the HS-HEA sample; (C) LUR stress-strain curves of HM-HEA and HS-HEA; (D) The evolution of calculated HDI stress versus true strain. HEAs: High-entropy alloys; HEA: high-entropy alloy; HS: heterogeneous structure; HM: homogenized; SEM: scanning electron microscope; LUR: loading-unloading-reloading; HDI: hetero-deformation induced.

shown by the typical LUR cycle curves, the HS-HEA exhibits larger unloading-reloading hysteresis loops than HM-HEA, signifying the appearance of a stronger Bauschinger effect. It is generally believed that the Bauschinger effect correlates with the HDI stress induced by heterogeneous plastic deformation. Accordingly, the HDI stress can be computed by unloading yield stress and reloading yield stress by analyzing the hysteresis loops[28]. Figure 3D plots the HDI stress versus true strain for both HS-HEA and HM-HEA. With the tensile deformation proceeding, the HDI stress of HS-HEA increases even more dramatically throughout all strains compared to HM-HEA. This strong HDI stress would trigger an extra HDI hardening mechanism during plastic deformation, which is responsible for enhanced strength without sacrificing ductility.

Microstructure evolution during tensile deformation

To further reveal the reasons for the remarkable HDI strengthening response of the HS-HEA, microstructure evolution at various interrupted strains was systematically examined. Figure 4 shows the deformed substructures of HS-HEA after deforming to 10% strain. HCP lamellae emerged prominently within the non-recrystallized FCC zones, as depicted in the IPF map [Figure 4A], phase map [Figure 4B], and the corresponding electron channeling contrast (ECC) image [Figure 4C]. These parallel HCP lamellae

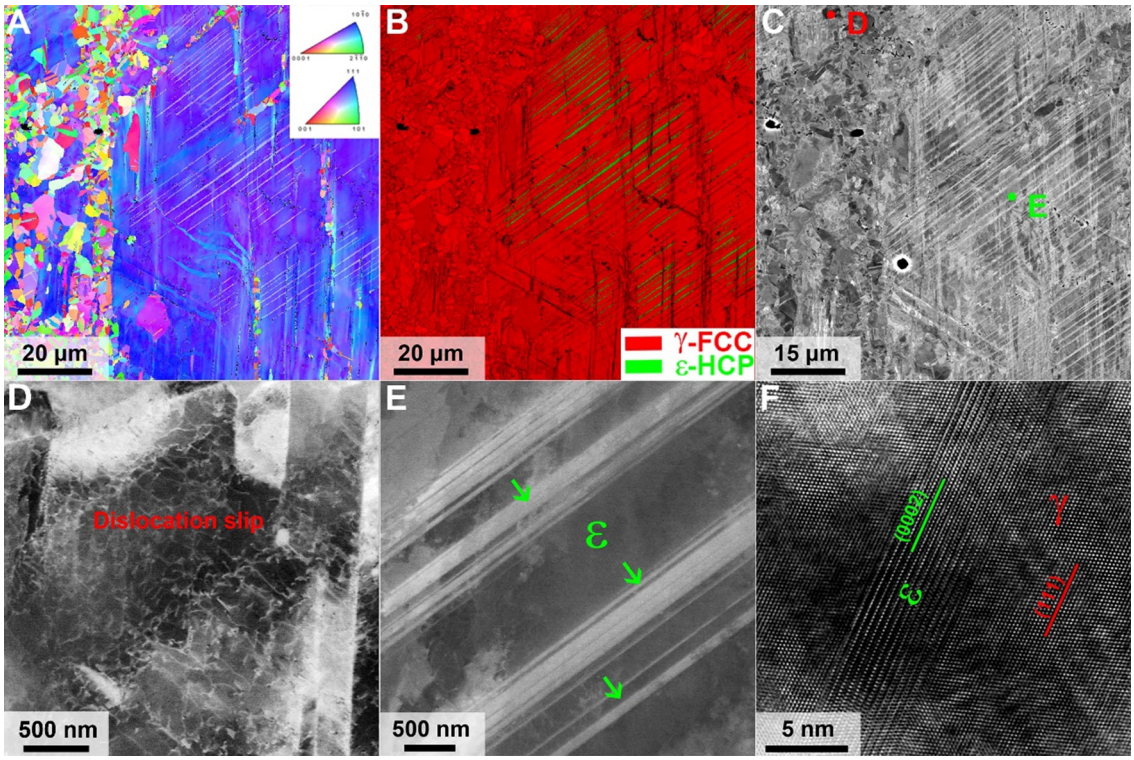

Figure 4. Heterogeneous martensite phase transformation in the HS-HEA at 10% strain. (A) IPF map; (B) Phase map overlayed with IQ map; (C) ECC image; (D and E) Zoom-in ECC images of the marked zone in (C); (F) High-resolution TEM image showing the atomic structure of FCC and HCP phases. EBSD maps and the corresponding ECC image indicate the martensite phase transformation from FCC to HCP occurs in the non-recrystallized zone, forming the lamellar plates, whereas dislocation slip dominates in the recrystallized zone. This suggests heterogeneous deformation behavior in our HS-HEA. The deformation-induced HCP phase obeys the S-N orientation relationship with the FCC matrix. HS: Heterogeneous structure; HEA: high-entropy alloy; IPF: inverse pole figure; IQ: image quality; ECC: electron channeling contrast; TEM: transmission electron microscopy; FCC: face-centered cubic; HCP: hexagonal close-packed; EBSD: electron backscatter diffraction.

[Figure 4E], attributable to deformation-induced martensitic transformation, stopped at the boundaries of recrystallized areas. The HR-TEM image in Figure 4F further unravels the $(0001)_{HCP}//\{111\}_{FCC}$ and $\langle 11\bar{2}0\rangle_{HCP}//\langle 110\rangle_{FCC}$ Shoji-Nishiyama (S-N) orientation relationship between these two phases. In contrast, the ECC image in Figure 4D shows that the deformation of adjacent recrystallized zones is governed by dislocation slip, conspicuously devoid of any HCP phase. Dislocations primarily exhibit a planar arrangement and inevitably entangle with each other as the dislocation density increases. It is worth noting that the grain size remains largely inconsequential in the current study. Regardless of grain size variation from 12 to 41 um, dislocation activities dominate up to the medium stage of deformation (~30% strain), with HCP martensite typically manifesting at a very large strain[29]. In short, depending on the densities of pre-existing dislocations, fundamentally different martensitic phase transformation capabilities are shown between non-recrystallized and recrystallized zones, despite the lack of SFE variation in our HS-HEA. Such surprising heterogeneous martensite phase transformation is a phenomenon unreported in metastable materials[19].

Upon reaching a medium strain level of 30%, the deformation within recrystallized zones predominantly arises from dislocation slip, while marked HCP lamellae form in the non-recrystallized counterparts, as shown in Figure 5A and B. Thus, the attractive heterogeneous deformation between non-recrystallized and recrystallized zones sustains with increasing strain. A surge in HCP lamellae results in their interaction with

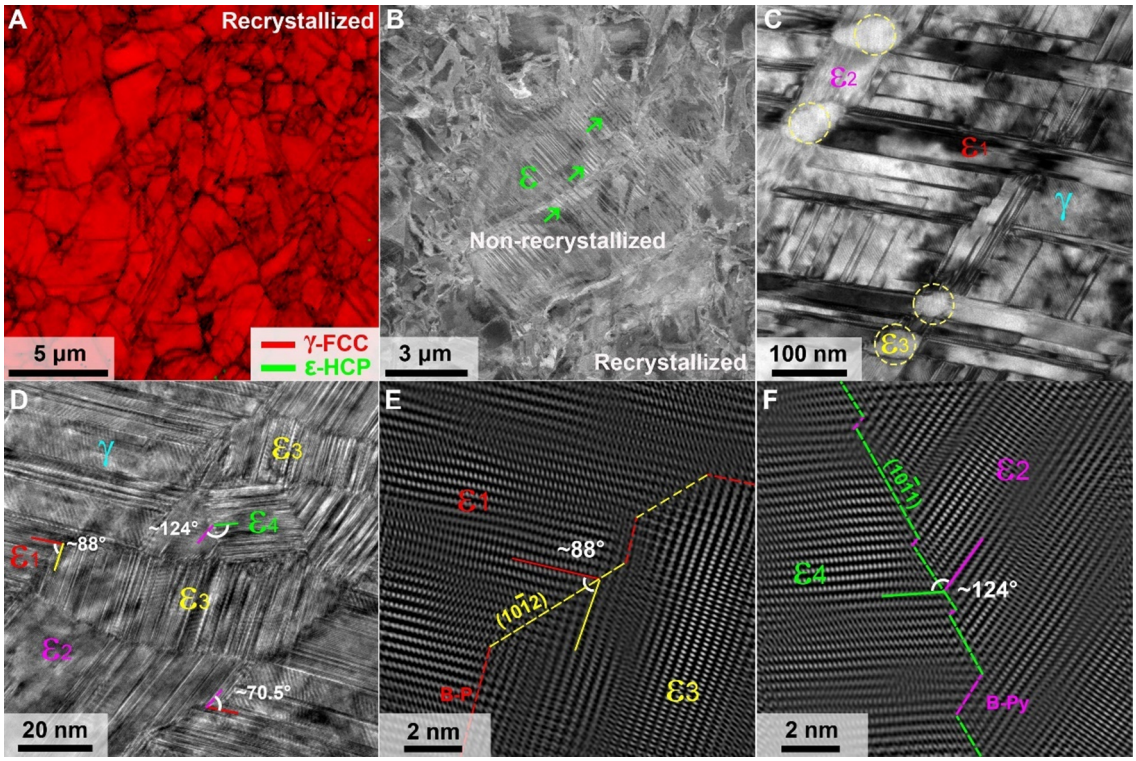

Figure 5. Sustained heterogeneous deformation substructures in the HS-HEA at 30% strain. (A) EBSD phase map overlayed IQ maps in the recrystallized zones; (B) ECC image showing the heterogeneous deformation behavior between the recrystallized and non-recrystallized zones; (C) The BF-TEM image indicating HCP interactions in the non-recrystallized zone. $\varepsilon_{(1\text{-}4)}$ represent HCP variants with different orientations, while γ represents the FCC matrix; (D) The HR-TEM image of the HCP intersections area; (E and F) The fast Fourier transform filtered HR-TEM image of the boundary structure marked in (D). The orientation of ε phases at junction areas is marked, which indicates {10$\bar{1}$2} and {10$\bar{1}$1} twinning relationships. HS: Heterogeneous structure; HEA: high-entropy alloy; EBSD: electron backscatter diffraction; IQ: image quality; ECC: electron channeling contrast; BF: bright field; TEM: transmission electron microscopy; HCP: hexagonal close-packed; FCC: face-centered cubic; HR: high-resolution.

one another (see Figure 5C), which was not observed in the fully recrystallized HEA even at high strains[29]. This distinct behavior stems from phase transformation being constrained within localized non-recrystallized zones. The intersecting HCP variants exhibited an orientation relationship of 70.5°⟨11$\bar{2}$0⟩ [Figure 5D], which transform through varied {111} planes in the FCC crystal that obey the common S-N relationship with the matrix, forming net structures at junction areas. Noteworthy, HRTEM observations in Figure 5E and F also indicate the twinning relationship among these HCP variants at junction areas. They show two types of ~88°⟨11$\bar{2}$0⟩ (ε_1 with ε_3) and ~56°⟨11$\bar{2}$0⟩ (ε_2 with ε_4), which obey {10$\bar{1}$2} and {10$\bar{1}$1} twinning relationships in HCP crystals, respectively. Two types of HCP twins are the intersection products of martensite variants with different habit planes[30]. Both coherent twin boundaries and incoherent twin boundaries with a relationship (10$\bar{1}$0)ε_1//(0001)ε_3 (B-P) and (10$\bar{1}$1)ε_2//(0001)ε_4 (B-Py) are discerned in these HCP variants, as marked via dashed lines with different colors. These interaction and twinning relationships are typically observed in Fe-Mn-Si and Co-based alloys with low SFE (< 15 mJ/m^2)[30,31], yet are rarely reported in alloys with medium SFE (20-35 mJ/m^2), including metastable HEAs and TRIP steels[32,33].

When the strain goes up to 49%, we detect intensive HCP lamellae intersections based on ECCI observations in the non-recrystallized zones, while very fine HCP martensite plates are seen in the recrystallized zones, as depicted in Figure 6A-C. The further zoom-in TEM observations reveal abundant nanograins at intersections of the HCP lamellae that comprise both FCC and HCP phases. As shown by the

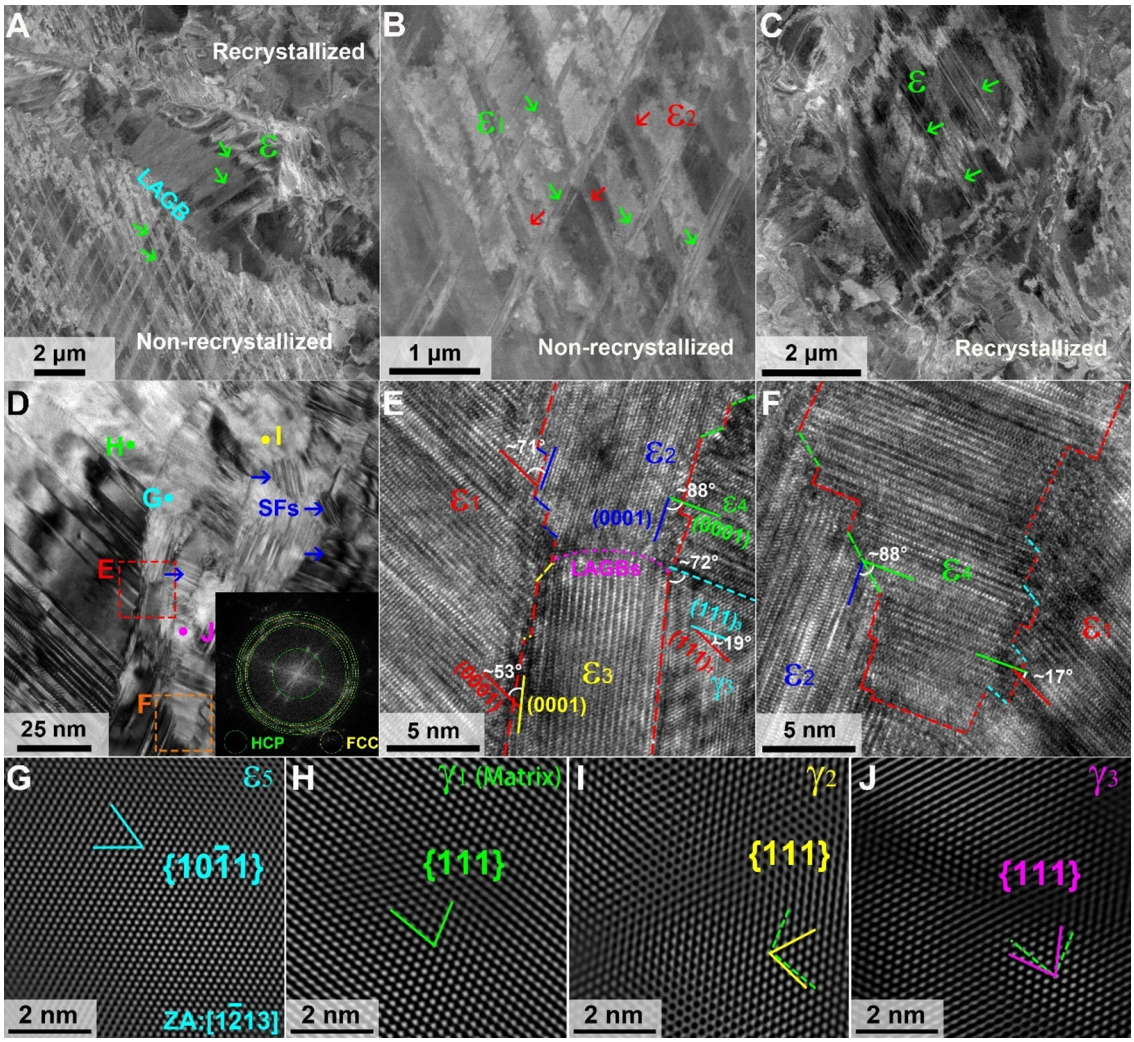

Figure 6. Deformation substructures of the HS-HEA at 49% strain. ECC images of HS-HEA showing (A) martensite emission from LAGBs, (B) ε-ε intersection in the non-recrystallized and (C) martensite in the recrystallized zone; (D) BF-TEM showing the dual-nanograins of the FCC and HCP phases at the junction area of the HCP lamellae. The selected area electron diffraction pattern confirms the formation of dual-nanograins. Stacking faults are detected inside nanograins; (E and F) Zoom-in HR-TEM images showing ε variants of the marked zone in (D); (G-J) The FFT-filtered HR-TEM images of ε and γ variants in (D). $\varepsilon_{(1\text{-}5)}$ and $\gamma_{(1\text{-}3)}$ represent HCP and FCC variants with different orientations, respectively, of which the specific orientation among them is marked in images. HS: Heterogeneous structure; HEA: high-entropy alloy; ECC: electron channeling contrast; LAGBs: low-angle grain boundaries; BF: bright field; FCC: face-centered cubic; HCP: hexagonal close-packed; HR: high-resolution; FFT: fast Fourier transform.

inserted fast Fourier transform image (inset in Figure 6D), diffraction rings with various crystal orientations signify the existence of nanograins. The further HRTEM images reveal, beyond the aforementioned twinning relationship [Figure 6E and F], the existence of an HCP variant with a 53°$\langle 11\bar{2}0\rangle$ (ε_3 with ε_1), indicating a 3° deviation from the {10$\bar{1}$1} twinning (typically measured as 56°) due to the grain rotation during deformation [Figure 6G]. In addition to HCP variants, we detect the unexpected formation of FCC variants (γ_2) with a twinning relationship to the FCC matrix (γ_1) in Figure 6H and I. Given that the representative lamellae shape for twinning in FCC materials is absent here, the special twin relationship here is formed via reverse phase transformation from ε to γ at this high strain level. We also detect another γ_3 FCC variant with ~19°$\langle 110\rangle$ with the FCC matrix γ_1, obeying the S-N orientation relationship with both ε_3 and ε_4 martensite variants [Figure 6J]. This implies that γ_3 was transformed from either ε_3 or ε_4, which is another evidence of reverse martensitic phase transformation. Figure 6D-F shows that both FCC and HCP

nanograins contain a high density of stacking faults (SFs) throughout whole grains, which were generated by the emission of partial dislocations from twin boundaries.

Besides the twinning or S-N orientation relationship, an FCC nanograin with another orientation relationship is exhibited, as shown in Figure 7A. The FCC nanograin shows $(0001)_{HCP}//\{001\}_{FCC}$ and $\langle 11\bar{2}0\rangle_{HCP}//\langle 110\rangle_{FCC}$ with ε_2, see Figure 7B. This is close to the S-N orientation relationship yet with a ~14° mismatch, which is due to the grain orientation. During deformation, the two directional ε phases interacted with each other and the ε_1 reversely transformed to FCC with a twin relationship. When the grain size refines at the nanoscale, grain rotation and partial dislocations are commonly seen to coordinate plastic strain. Thus, a slight ~14° mismatch to the twinning relationship is found due to the grain rotation, as indicated in Figure 7C and D. In the current study, grain rotation accounts for the slight deviation from the ideal type of orientation relationship in both FCC and HCP variants. Table 1 summarizes all the relationships between these variants and their possible formation mechanisms.

Dislocation-mediated heterogeneous martensitic transformation

In this work, we demonstrate the dislocation-mediated heterogeneous martensitic transformation in a partially recrystallized high-entropy alloy. This heterogeneous martensitic phase transformation is induced by pre-existing partial dislocations in non-recrystallized zones. The difference in deformation behavior between recrystallized and non-recrystallized zones persists until the later stages of strain. The formation mechanisms of this heterogeneous martensitic transformation at various strain levels are discussed in detail below.

At the early deformation stage, martensitic transformation occurs only in localized non-recrystallized zones upon tensile loading, while adjacent recrystallized zones deform through dislocation slip, resulting in the presence of heterogeneous martensite. To further uncover the underlying mechanism of the heterogeneous phase transformation in the non-recrystallized zones, we performed molecular dynamic (MD) simulations by applying a tension load to a layered structure featuring two LAGBs with a misorientation angle of 10° [Figure 8]. The relaxed LAGBs are randomly decorated with dislocations [Figure 8A-C]. Upon loading, Shockley partial dislocations emit from the two LAGBs and glide along the $(11\bar{1})$ plane, culminating in an array of SFs [Figure 8D and E]. As tensile strain increases, the continuous emission of these partial dislocations facilitates FCC-HCP martensite phase transformation [Figure 8F-H]. This transformation is consistent with the known mechanism of partial dislocation emissions on alternating slip planes[34], corroborated by the S-N relationship between the FCC and HCP phases observed in Figure 8I, and consistent with experimental findings in Figure 4F. Our MD simulations highlight that both pre-existing dislocations and LAGBs act as prolific sources of partial dislocations, catalyzing the emergence of HCP martensite as deformation advances.

As deformation progresses to medium strain levels, the heterogeneity of martensitic phase transformation endures. During this stage, dislocation density increases in the recrystallized zones, while multiple HCP variants are activated in the non-recrystallized zones [Figure 5]. The ε-martensite phase forms through the successive gliding of partial dislocations on alternating {111} plane[35]. When partial dislocations initiate from conjugate {111} planes within the FCC matrix, the resulting HCP variants intersect at a misorientation angle of around 70.5° [Figure 5C]. Partial dislocations within one HCP plate are generally hindered from propagating into the slip system of an intersecting HCP plate due to severe stress concentration from dislocation pile-up at intersections[36,37]. To accommodate the resulting plastic deformation, twinning is commonly an effective mechanism in hexagonal phases. Thus, intersections of two crossing HCP phases can generate ε-martensite twins to relieve local stress, governed by the orientation of crossing shear

Table 1. The summary of the orientation relationship of the FCC and HCP phases

Relationships	Formation
ε-ε	
70.5°⟨11$\bar{2}$0⟩	Two ε transformed from different planes of {111} group in FCC crystal.
88°⟨11$\bar{2}$0⟩	{10$\bar{1}$2} twin relationships
56°⟨11$\bar{2}$0⟩	{10$\bar{1}$1} twin relationships
53°⟨11$\bar{2}$0⟩	{10$\bar{1}$1} twin relationships+grain rotation
⟨11$\bar{2}$0⟩//⟨11$\bar{2}$3⟩	Grain rotation
γ-γ	
70.5°⟨110⟩	FCC twin relationships via reverse transformation
19°⟨110⟩	Reverse transformation from ε {10$\bar{1}$2} twin
54°⟨110⟩	Reverse phase transformation + grain rotation

FCC: Face-centered cubic; HCP: hexagonal close-packed.

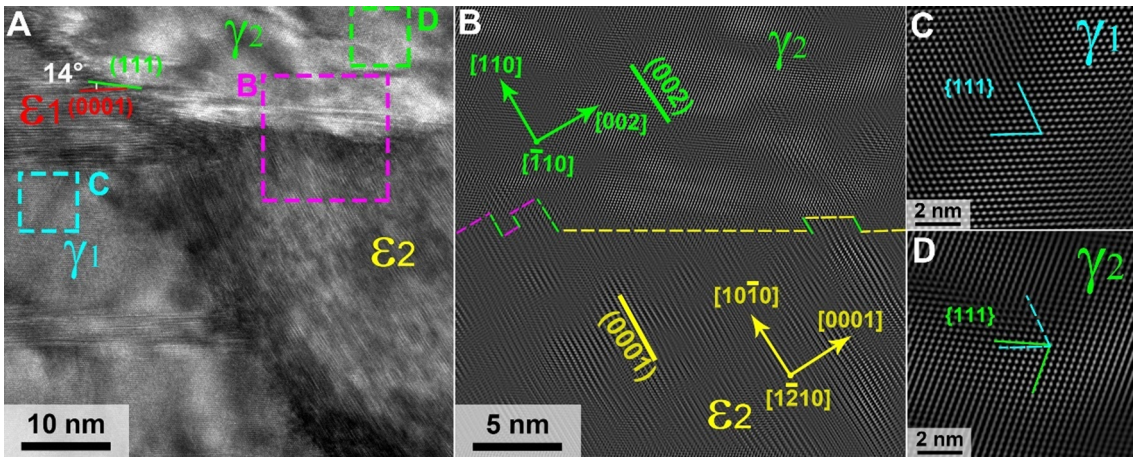

Figure 7. (A) HR-TEM image of HS-HEA with 49% strain showing new γ variant at interaction areas; (B-D) The FFT-filtered HR-TEM image marked in (A) showing orientation relationships between γ and ε variants. HR: High-resolution; TEM: transmission electron microscopy; HS: heterogeneous structure; HEA: high-entropy alloy; FFT: fast Fourier transform.

systems[38]. When the HCP variants present the orientation relationships of ~88°⟨11$\bar{2}$0⟩ and ~56°⟨11$\bar{2}$0⟩, {10$\bar{1}$2} and {10$\bar{1}$1} twins are produced. These twinning processes are mainly attributed to the collision of different habit plane variants depending on the directions of crossing shear systems. Specifically, incident shear forces aligned at either 90° or 30° relative to the intersection axis are responsible for forming {10$\bar{1}$2} and {10$\bar{1}$1} twins, respectively[30], as shown in Figure 5E and F. The formation of ε-twins in the non-recrystallized zones with increasing strain further reinforces the heterogeneous structure.

Even at higher strain (~49% strain), the heterogeneous deformation behavior still persists. In the recrystallized zones, the mechanical driving force can reach the stress required for martensitic transformation due to the increased flow stress, resulting in the formation of very fine martensite phases [Figure 6C]. Meanwhile, intersections of two HCP bands in the non-recrystallized zones become increasingly complex [Figure 6D] as stress on the HCP plates rises. Partial dislocations can emit from the interfaces of multiple martensite phases. When double half-partial dislocations (1/12⟨1$\bar{1}$2⟩) glide on the conjugated shear systems, fresh FCC phases form by reverse transformation from the HCP martensite [Figures 6 and 7][39,40]. Based on the diversity in orientations of HCP variants, the newly generated FCC phases exhibit complex orientation relationships with the FCC matrix, as shown in Table 1. The formation

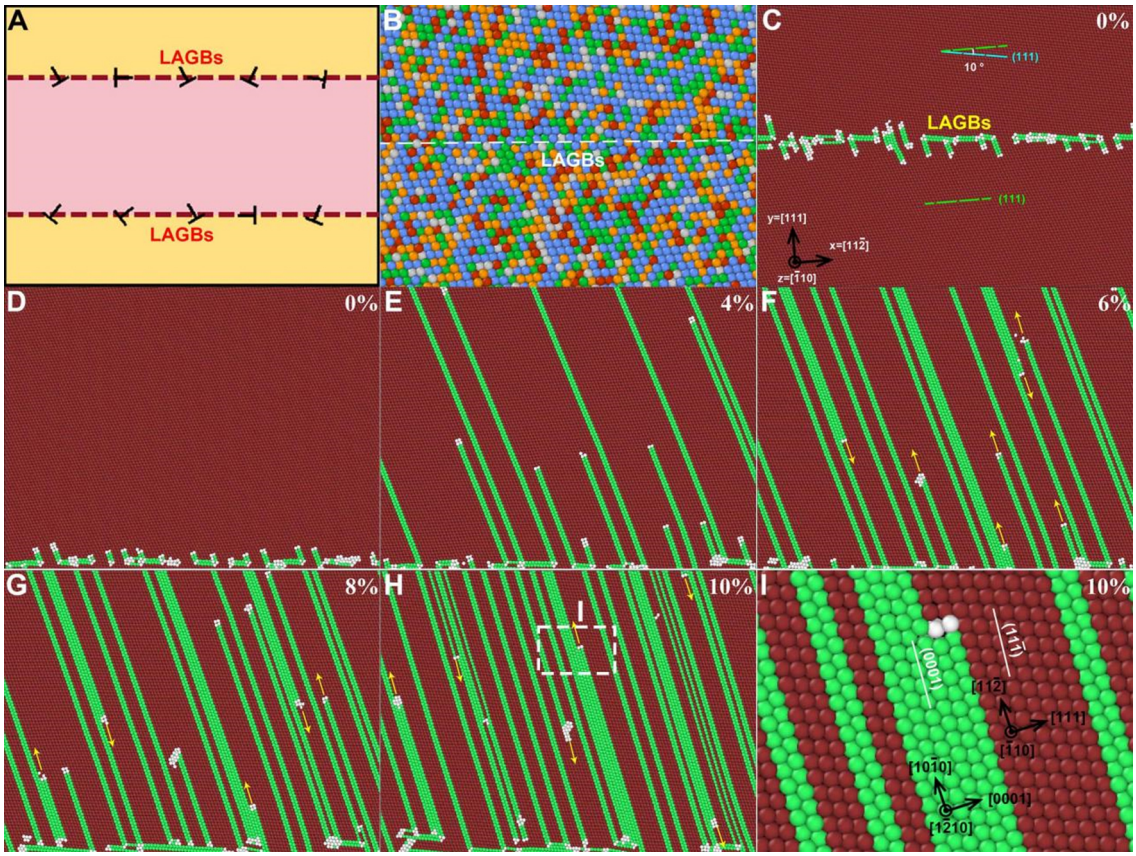

Figure 8. MD simulations revealing dislocation-mediated martensite phase transformation. (A) Schematic of the simulation model with two LAGBs (dashed lines). "T" symbols indicate dislocations at LAGBs; (B) Random distribution of various elements in the model and (C) atomic structure of relaxed LAGB. The misorientation between LAGB is about 10°; (D-H) The FCC-HCP phase transformation with increasing strain: (D) 0%, (E) 4%, (F) 6%, (G) 8%, and (H) 10%; (I) The magnified image of (H) showing the orientation relationship between the HCP and FCC phases. The atoms are colored according to common neighbor analysis. The arrows indicate the glide direction of the partial dislocations. MD: Molecular dynamic; LAGBs: low-angle grain boundaries; LAGB: low-angle grain boundary; FCC: face-centered cubic; HCP: hexagonal close-packed.

of dual-nanograins composed of FCC and HCP phases in the non-recrystallized zones effectively facilitates persistent heterogeneous deformation through the later stages of plastic deformation.

Overall, we instigate heterogeneous martensitic phase transformation by meticulously introducing LAGBs and dislocations, presenting an alternative approach to realize the TRIP effect. Both dislocations and LAGBs supply the necessary sites for the emission of partial dislocations upon straining, facilitating the formation of HCP plates. Traditionally, efforts to achieve the TRIP effect have focused on manipulating SFE, typically by altering chemical compositions or reducing loading temperatures[35,41]. In materials with reduced SFE, martensitic phase transformations readily occur[17,42,43], attributed to the decreased energy barrier for activating partial dislocations[44,45]. By contrast, we circumvent the SFE limitation and enable the martensitic phase transformation at the onset of deformation, which was deemed elusive for materials with such a level of SFE (~20 mJ/m^2) previously[46]. This distinctive martensitic phase transformation effectively promotes heterogeneous deformation behavior in HS-HEA.

Sustainable hetero-deformation induced hardening

The strain hardening rates are significantly higher in the HS-HEA compared to the HM-HEA, which is essential for achieving enhanced strength-ductility synergy, as shown in Figure 3A and B. The contribution

to the superior strain hardening capability of HS-HEA is its higher HDI stress relative to HM-HEA. Notably, HDI stress increases with applied tensile strain [Figure 3C and D], driven primarily by the sustained heterogeneous deformation behavior across all strain stages. This includes early-stage martensitic transformation and later-stage dual-nanograin formation at HCP lamellae intersections in the non-recrystallized zones, while dislocation motion consistently dominates in the recrystallized zones.

To investigate the origin of HDI stress further, nanoindentation was used to assess the hardness of recrystallized and non-recrystallized zones across various strain stages [Figure 9]. As shown in Figure 9A, D, and G, non-recrystallized zones exhibit higher strength than recrystallized zones in the undeformed state due to dislocation strengthening. Under applied tensile stress, the strength of both zones experiences distinct increments [Figure 9B, E and H]. The softer recrystallized zones deform preferentially compared to the harder non-recrystallized zones, resulting in steep strain gradients within the material. To accommodate deformation under complex stress/strain conditions, numerous geometrically necessary dislocations (GNDs) are generated and accumulate at the interfaces[47,48]. The pile-up of GNDs produces back stress in the soft zones and forward stress in the hard zones, collectively contributing to HDI stress and substantially enhancing strength and hardening[49,50]. With increasing tensile strain, the hardness contrast between zones persists even at higher deformation levels (up to 30% strain, Figure 9C, F, and I), driven by localized martensitic phase transformation within the non-recrystallized zones. This observation provides a compelling explanation for the continuous rise in HDI stress throughout early and medium strain stages in HS-HEA [Figure 3C and D], differing from prior studies on heterostructured materials, where HDI stress increase typically diminishes during plastic deformation[51].

These findings indicate that achieving substantial heterogeneous deformation behavior promotes both enhanced strength and strain hardening, attributes critical for high-performance structural materials. Such unique deformation behavior manifests in three key aspects: (1) The non-recrystallized zones with a high density of dislocations tend to soften upon loading due to dislocation recovery[51,52]. Our strategy takes advantage of dislocation to trigger martensitic phase transformation, which avoids the possible softening and, instead, offers strain hardening from this phase transformation from FCC to HCP; (2) The martensitic phase transformation is confined in the non-recrystallized zones, whereas the recrystallized zones are deformed by dislocation slip, which leads to the pile-ups of HCP lamellae at the boundaries between these two zones [Figure 4A-C]. This heterogeneous deformation behavior gives rise to high HDI stress during deformation, thereby enhancing the strain hardening [Figure 3B and D]; (3) The localized martensitic phase transformation produces a large number of dual-nanograins at HCP intersections. This prevents stress concentration in these relatively harder zones and further avoids the possible crack nucleation. Together, these mechanisms underpin the superb mechanical properties observed in our HS-HEA.

CONCLUSIONS

We demonstrate a new approach to designing heterostructured materials through dislocation-mediated martensitic phase transformation. The martensitic phase reaction from FCC to HCP is triggered by the pre-existing dislocations in non-recrystallized zones, which provides partials whose slip on alternative planes result in the phase transformation, while the resulting localized phase transformations yield dual-nanograins at HCP lamellae intersections as strain levels increase. These features collectively contribute to a significant enhancement in the heterogeneous deformation behavior. The proposed strategy effectively exploits the strong strengthening and strain hardening from the HDI hardening, delivering attractive mechanical performance in our HEA. Our findings provide a novel perspective on harnessing heterogeneous deformation behavior to develop high-performance structural materials.

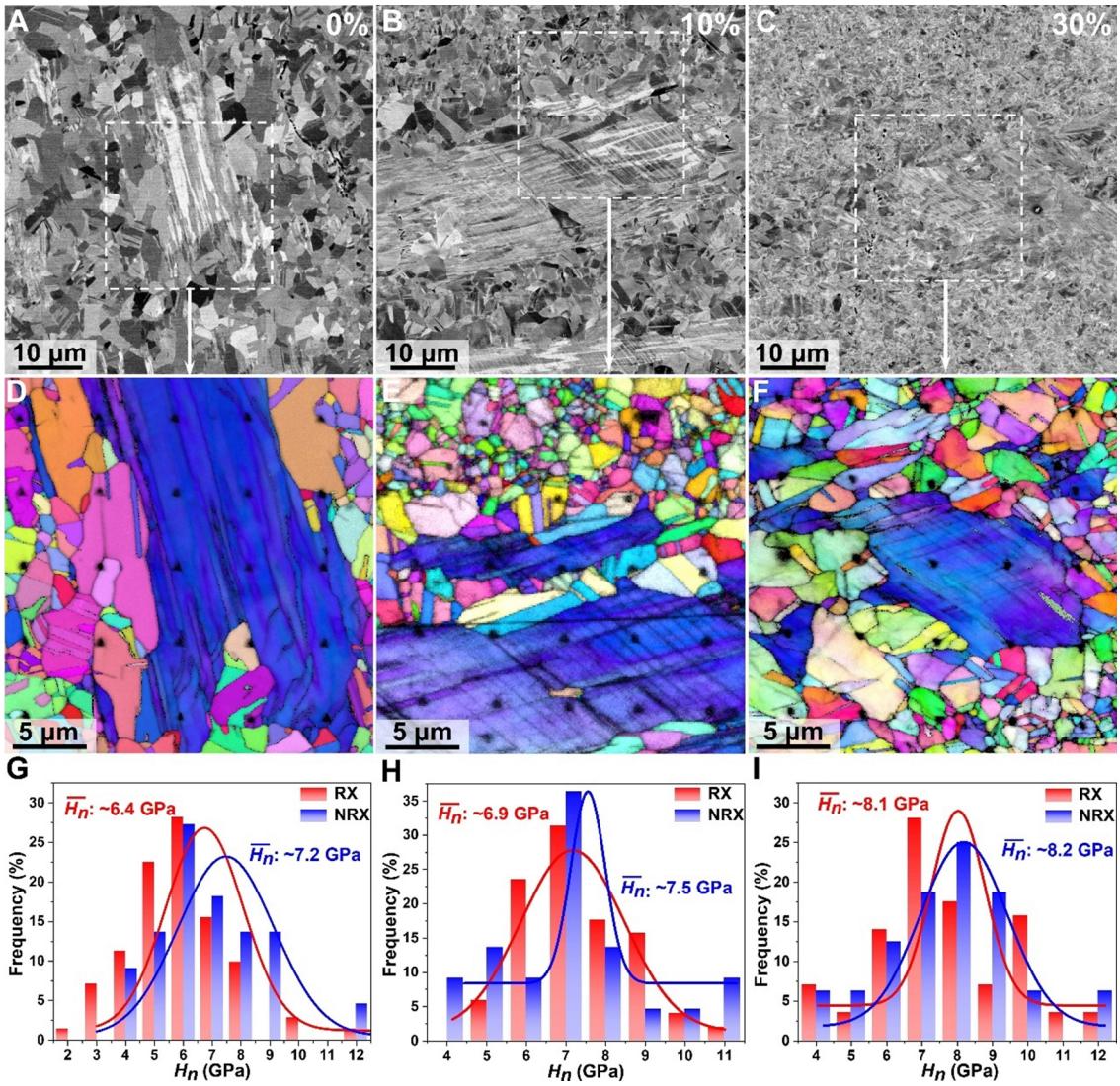

Figure 9. Nanoindentation analysis of the HS-HEA at 0%, 10%, and 30% plastic strain. (A-C) The ECC micrograph revealing the microstructure evolution; (D-F) Representative EBSD IPF images overlayed IQ maps showing nano-indents in both recrystallized (RX) and non-recrystallized (NRX) zones, respectively; (G-I) The distribution of nanoindentation hardness (H_n) in RX and NRX zones. $\overline{H_n}$, average nanoindentation hardness. HS: Heterogeneous structure; HEA: high-entropy alloy; ECC: electron channeling contrast; EBSD: electron backscatter diffraction; IPF: inverse pole figure; IQ: image quality.

DECLARATIONS

Authors' contributions

Writing - original draft, conceptualization, investigation, data curation: Wang, F.

Writing - original draft, resources, data curation, investigation: An, X.

Writing - review & editing, conceptualization, supervision, funding acquisition: Wang, Z.

Investigation, data curation: Wu, W.; Xia, W.

Investigation, supervision: Ni, S.; Gu, J.

Investigation, data curation: Yi, J.

Validation, supervision: Yang, Y.

Writing - review & editing, conceptualization, supervision, funding acquisition: Song, M.; Zhu, Y.

Availability of data and materials

The data supporting the findings of this study are available within this Article and its Supplementary Materials. Further data are available from the corresponding authors upon reasonable request.

Financial support and sponsorship

Song, M. and Wang, Z. acknowledge support from the National Key Research and Development Program of China (2022YFE0134400). Song, M. acknowledges support from the Science and Technology Innovation Program of Hunan Province (No. 2022RC3035). Wang, Z. acknowledges the support from the Natural Science Foundation of Hunan Province (Grant No. 2022JJ30712) and Double Cs-corrected TEM in State Key Laboratory of Powder Metallurgy. Institute for Advanced Study of Central South University and Hunan Center for Electron Microscopy are sincerely appreciated for TEM technical support. Zhu, Y. acknowledges the support of the National Natural Science Foundation of China (51931003) and the Hong Kong Research Grants Council (GRF 11214121).

Conflicts of interest

Zhu, Y. is the Guest Editor of the Special Issue "Heterostructures for Superior Properties" and a Senior Editorial Board member of the journal *Microstructures*. Zhu, Y. was not involved in any steps of editorial processing, notably including reviewer selection, manuscript handling, or decision making. The other authors declared that there are no conflicts of interest.

Ethical approval and consent to participate

Not applicable.

Consent for publication

Not applicable.

REFERENCES

1. Sathiyamoorthi, P.; Kim, H. S. High-entropy alloys with heterogeneous microstructure: processing and mechanical properties. *Prog. Mater. Sci.* **2022**, *123*, 100709. DOI
2. Ma, E.; Zhu, T. Towards strength-ductility synergy through the design of heterogeneous nanostructures in metals. *Mater. Today.* **2017**, *20*, 323-31. DOI
3. Park, H. K.; Kim, Y.; Jung, J.; et al. Efficient design of harmonic structure using an integrated hetero-deformation induced hardening model and machine learning algorithm. *Acta. Mater.* **2023**, *244*, 118583. DOI
4. Tang, X.; Peng, Q.; Long, J.; et al. Recent progress on plastic forming of laminated metal composites: processes, heterogeneous deformation, and interfacial regulation. *J. Mater. Sci. Technol.* **2025**, *229*, 67-91. DOI
5. Shen, J.; Choi, Y. T.; Yang, J.; et al. Fabrication of spatially-variable heterostructured CoCrFeMnNi high entropy alloy by laser processing. *Mat. Sci. Eng. A.* **2024**, *896*, 146272. DOI
6. Zhang, C.; Zhu, C.; Cao, P.; et al. Aged metastable high-entropy alloys with heterogeneous lamella structure for superior strength-ductility synergy. *Acta. Mater.* **2020**, *199*, 602-12. DOI
7. Fang, T. H.; Li, W. L.; Tao, N. R.; Lu, K. Revealing extraordinary intrinsic tensile plasticity in gradient nano-grained copper. *Science* **2011**, *331*, 1587-90. DOI PubMed
8. Pan, Q. S.; Long, J. Z.; Jing, L. J.; Tao, N. R.; Lu, L. Cyclic strain amplitude-dependent fatigue mechanism of gradient nanograined Cu. *Acta. Mater.* **2020**, *196*, 252-60. DOI
9. Zhang, B. H.; Chen, J.; Wang, P. F.; Sun, B. T.; Cao, Y. Enhanced strength-ductility of CoCrFeMnNi high-entropy alloy with inverse gradient-grained structure prepared by laser surface heat-treatment technique. *J. Mater. Sci. Technol.* **2022**, *111*, 111-9. DOI
10. Cheng, Z.; Zhou, H.; Lu, Q.; Gao, H.; Lu, L. Extra strengthening and work hardening in gradient nanotwinned metals. *Science* **2018**, *362*, eaau1925. DOI PubMed
11. Wei, Y.; Li, Y.; Zhu, L.; et al. Evading the strength-ductility trade-off dilemma in steel through gradient hierarchical nanotwins. *Nat. Commun.* **2014**, *5*, 3580. DOI PubMed PMC

12. Pan, Q.; Zhang, L.; Feng, R.; et al. Gradient cell-structured high-entropy alloy with exceptional strength and ductility. *Science* **2021**, *374*, 984-9. DOI
13. Shi, P.; Ren, W.; Zheng, T.; et al. Enhanced strength-ductility synergy in ultrafine-grained eutectic high-entropy alloys by inheriting microstructural lamellae. *Nat. Commun.* **2019**, *10*, 489. DOI PubMed PMC
14. Du, X. H.; Li, W. P.; Chang, H. T.; et al. Dual heterogeneous structures lead to ultrahigh strength and uniform ductility in a Co-Cr-Ni medium-entropy alloy. *Nat. Commun.* **2020**, *11*, 2390. DOI PubMed PMC
15. Cao, S.; Liu, H.; Jiang, J.; et al. Effect of heat treatment on gradient microstructure and tensile property of laser powder bed fusion fabricated 15-5 precipitation hardening stainless steel. *Acta. Metall. Sin.* **2024**, *37*, 181-95. DOI
16. Grässel, O.; Krüger, L.; Frommeyer, G.; Meyer, L. W. High strength Fe-Mn-(Al, Si) TRIP/TWIP steels development - properties - application. *Int. J. Plast.* **2000**, *16*, 1391-409. DOI
17. Li, Z.; Körmann, F.; Grabowski, B.; Neugebauer, J.; Raabe, D. Ab initio assisted design of quinary dual-phase high-entropy alloys with transformation-induced plasticity. *Acta. Mater.* **2017**, *136*, 262-70. DOI
18. Liu, S. F.; Wu, Y.; Wang, H. T.; et al. Stacking fault energy of face-centered-cubic high entropy alloys. *Intermetallics* **2018**, *93*, 269-73. DOI
19. Liu, S.; Wu, Y.; Wang, H.; et al. Transformation-reinforced high-entropy alloys with superior mechanical properties via tailoring stacking fault energy. *J. Alloys. Compd.* **2019**, *792*, 444-55. DOI
20. Sohrabi, M. J.; Mehranpour, M. S.; Heydarinia, A.; et al. Deformation-induced martensitic transformation kinetics in TRIP-assisted steels and high-entropy alloys. *Acta. Mater.* **2024**, *280*, 120354. DOI
21. Guo, N.; Zhang, Z.; Dong, Q.; et al. Strengthening and toughening austenitic steel by introducing gradient martensite via cyclic forward/reverse torsion. *Mater. Design.* **2018**, *143*, 150-9. DOI
22. Cao, S. C.; Liu, J.; Zhu, L.; et al. Nature-inspired hierarchical steels. *Sci. Rep.* **2018**, *8*, 5088. DOI PubMed PMC
23. Plimpton, S. Fast parallel algorithms for short-range molecular dynamics. *J. Comput. Phys.* **1995**, *117*, 1-19. DOI
24. Li, Z.; Pradeep, K. G.; Deng, Y.; Raabe, D.; Tasan, C. C. Metastable high-entropy dual-phase alloys overcome the strength-ductility trade-off. *Nature* **2016**, *534*, 227-30. DOI PubMed
25. Ding, Q.; Zhang, Y.; Chen, X.; et al. Tuning element distribution, structure and properties by composition in high-entropy alloys. *Nature* **2019**, *574*, 223-7. DOI PubMed
26. Hasan, M. N.; Liu, Y. F.; An, X. H.; et al. Simultaneously enhancing strength and ductility of a high-entropy alloy via gradient hierarchical microstructures. *Int. J. Plast.* **2019**, *123*, 178-95. DOI
27. Courtney, T.H. *Mechanical behavior of materials*, Waveland Press, 2005.
28. Yang, M.; Yan, D.; Yuan, F.; Jiang, P.; Ma, E.; Wu, X. Dynamically reinforced heterogeneous grain structure prolongs ductility in a medium-entropy alloy with gigapascal yield strength. *Proc. Natl. Acad. Sci. U. S. A.* **2018**, *115*, 7224-9. DOI PubMed PMC
29. Chen, W.; An, X.; Wang, Z.; Li, Y.; Gu, J.; Song, M. Grain size dependent deformation behavior of a metastable Fe40Co20Cr20Mn10Ni10 high-entropy alloy. *J. Alloys. Compd.* **2021**, *883*, 160876. DOI
30. Zhang, X.; Sawaguchi, T. Twinning of deformation-induced ε-martensite in Fe-30Mn-6Si shape memory alloy. *Acta. Mater.* **2018**, *143*, 237-47. DOI
31. Martinez, M.; Hug, E. Characterization of deformation twinning in polycrystalline cobalt: a quantitative analysis. *Materialia* **2019**, *7*, 100420. DOI
32. Wagner, C.; Laplanche, G. Effects of stacking fault energy and temperature on grain boundary strengthening, intrinsic lattice strength and deformation mechanisms in CrMnFeCoNi high-entropy alloys with different Cr/Ni ratios. *Acta. Mater.* **2023**, *244*, 118541. DOI
33. Ponge, D.; MiUán, J.; Raabe, D. Design of lean maraging TRIP steels. In *Advanced Steels 2011, Proceedings of the ICAS*, Guilin, China, November 9-11, 2010; Weng, Y., Dong, H., Gan, Y., Eds.; Springer-Verlag: Berlin, Heidelberg, 2011; pp 199-208. DOI
34. Yang, X. S.; Sun, S.; Zhang, T. Y. The mechanism of bcc α' nucleation in single hcp ε laths in the fcc γ → hcp ε → bcc α' martensitic phase transformation. *Acta. Mater.* **2015**, *95*, 264-73. DOI
35. Soleimani, M.; Kalhor, A.; Mirzadeh, H. Transformation-induced plasticity (TRIP) in advanced steels: a review. *Mater. Sci. Eng. A.* **2020**, *795*, 140023. DOI
36. Shen, S.; Xie, P.; Wu, C. Temperature dependence of mechanical properties and deformation mechanism of Fe-25Mn-3Al-3Si alloy at high strain rate. *Mater. Sci. Eng. A.* **2023**, *872*, 144912. DOI
37. Su, J.; Wu, X.; Raabe, D.; Li, Z. Deformation-driven bidirectional transformation promotes bulk nanostructure formation in a metastable interstitial high entropy alloy. *Acta. Mater.* **2019**, *167*, 23-39. DOI
38. Singh, D.; Singh, A.; Sawaguchi, T. Elucidating deformation pathways and interface characteristic of self-accommodated dual γ/ε phase microstructure in Fe-Mn-Si-Al alloy. *Mater. Charact.* **2024**, *207*, 113521. DOI
39. Yang, J. H.; Wayman, C. M. Intersecting-shear mechanisms for the formation of secondary ϵ martensite variants. *Acta. Metall. Mater.* **1992**, *40*, 2025-31. DOI
40. Yang, J. H.; Wayman, C. M. On secondary variants formed at intersections of ϵ martensite variants. *Acta. Metall. Mater.* **1992**, *40*, 2011-23. DOI
41. Mishra, R. S.; Haridas, R. S.; Agrawal, P. High entropy alloys - tunability of deformation mechanisms through integration of compositional and microstructural domains. *Mater. Sci. Eng. A.* **2021**, *812*, 141085. DOI
42. Liu, J.; Luo, X.; Huang, B.; et al. Nano-twinning and martensitic transformation behaviors in 316L austenitic stainless steel during large tensile deformation. *Acta. Metall. Sin.* **2023**, *36*, 758-70. DOI

43. Huang, M.; Wang, L.; Wang, C.; et al. Optimizing crack initiation energy in austenitic steel via controlled martensitic transformation. *J. Mater. Sci. Technol.* **2024**, *198*, 231-42. DOI
44. Bu, Y.; Li, Z.; Liu, J.; Wang, H.; Raabe, D.; Yang, W. Nonbasal slip systems enable a strong and ductile hexagonal-close-packed high-entropy phase. *Phys. Rev. Lett.* **2019**, *122*, 075502. DOI
45. Chen, S.; Oh, H. S.; Gludovatz, B.; et al. Real-time observations of TRIP-induced ultrahigh strain hardening in a dual-phase CrMnFeCoNi high-entropy alloy. *Nat. Commun.* **2020**, *11*, 826. DOI PubMed PMC
46. Li, W.; Xie, D.; Li, D.; Zhang, Y.; Gao, Y.; Liaw, P. K. Mechanical behavior of high-entropy alloys. *Prog. Mater. Sci.* **2021**, *118*, 100777. DOI
47. Mughrabi, H. On the role of strain gradients and long-range internal stresses in the composite model of crystal plasticity. *Mater. Sci. Eng. A.* **2001**, *317*, 171-80. DOI
48. Liu, X. L.; Xue, Q. Q.; Wang, W.; et al. Back-stress-induced strengthening and strain hardening in dual-phase steel. *Materialia* **2019**, *7*, 100376. DOI
49. Kim, R. E.; Lee, J. H.; Haftlang, F.; et al. Hierarchical ferrous medium entropy with heterogeneous precipitates embedded in core-shell grain structure for superior mechanical properties. *Acta. Mater.* **2024**, *281*, 120397. DOI
50. Geng, X.; Gao, J.; Huang, Y.; et al. A novel dual-heterogeneous-structure ultralight steel with high strength and large ductility. *Acta. Mater.* **2023**, *252*, 118925. DOI
51. Wu, H.; Fan, G. An overview of tailoring strain delocalization for strength-ductility synergy. *Prog. Mater. Sci.* **2020**, *113*, 100675. DOI
52. Wu, S. W.; Wang, G.; Wang, Q.; et al. Enhancement of strength-ductility trade-off in a high-entropy alloy through a heterogeneous structure. *Acta. Mater.* **2019**, *165*, 444-58. DOI